RSC Advances

PAPER

View Article Online
View Journal | View Issue

Check for updates

Cite this: *RSC Adv.*, 2025, **15**, 17986

Photoelectrochemical properties of magnetic amine-based MIL-101(Cr) hybrid material and its application in the degradation of acebutolol in water†

Ngwako Joseas Waleng,[ac] Tshimangazo Saddam Munonde,[d] Anele Mpupa,[ac] Tshepiso Moremedi,[ac] Yongjun Zhang[e] and Philiswa Nosizo Nomngongo *[abc]

Received 20th April 2025
Accepted 19th May 2025

DOI: 10.1039/d5ra02767e

rsc.li/rsc-advances

Rapid advances in industries and agricultural practices have recently released various toxic pollutants into aquatic systems. Among other pollutants, pharmaceuticals, have been detected in environmental aquatic systems at levels that have negative health impacts on both humans and animals. This study employed an *in situ* chemical co-precipitation method to fabricate a magnetic amine-based metal organic framework nanocomposite. This nanocomposite was successfully synthesised and applied as a photocatalytic material for the mineralization of acebutolol (ACE) in water. The prepared materials, including the nanocomposite (Fe_3O_4@NH_2-MIL-101(Cr)) were characterised using transmission electron microscopy (TEM), Brunauer–Emmett–Teller (BET) analysis, Fourier transform infrared spectroscopy (FTIR) and X-ray powder diffraction (XRD). The optoelectronic properties were determined using photoluminescence (PL), electrochemical impedance spectroscopy, diffuse reflectance spectroscopy (UV-Vis DRS) and ultraviolet–visible spectroscopy. The photocatalytic efficacy of the nanocomposite was assessed *via* the degradation of acebutolol under visible light illumination. The results indicate that adsorption–desorption equilibrium was attained after 60 min in the dark, and 98.3% degradation efficiency was achieved after 180 min with the light on. According to scavenging experiments, superoxide radicals ($\cdot O_2^-$) were the main reactive oxygen species (ROS) during photodegradation. The Nyquist plot obtained from electrochemical impedance spectroscopy (EIS) showed that the Fe_3O_4@NH_2-MIL-101(Cr) nanocomposite had a reduced charge transfer resistance (R_{ct}), indicating separation and accelerated transfer of charges at the interface. The obtained electron lifespan (τ_e) supported the results, and was found to be higher for Fe_3O_4@NH_2-MIL-101(Cr) compared to NH_2-MIL-101(Cr) and pure Fe_3O_4. The photocatalytic mechanism revealed that the formed heterojunction followed a Z-scheme mechanism.

1. Introduction

Globally, access to clean and potable water has always been a societal concern. Major culprits in the contamination of environmental water include organic pollutants.[1] Pharmaceuticals are a major domain of contaminants of emerging concern (CEC) detected in aquatic systems.[2,3] These compounds are mainly used for medical purposes to sustain human health. Intact and metabolised forms of pharmaceuticals enter aquatic environments though various mechanisms, including direct disposal, hospital waste, human and veterinary use and pharmaceutical production plants.[4] Pharmaceuticals are not effectively retained by wastewater treatment plants (WWTPs) owing to their high polarity and water solubility.[5] Therefore, they have been detected in various environmental aquatic systems.[6–8] Their presence in the environment can pose a relatively high ecological risk, even at trace levels.[9] They can also cause some antimicrobial resistance in the environment, further threatening biodiversity.[10] β-Blockers are among the classes of pharmaceuticals that are intensively used, and their environmental effects are still under investigation. Acebutolol (ACE) is among the β-blockers that have been extensively used and can pose serious adverse effects when consumed at amounts up to ng L^{-1}. These include diarrhoea, shortness of breath,

---

[a] Department of Chemical Sciences, University of Johannesburg, Doornfontein Campus, P.O. Box 17011, Johannesburg, 2028, South Africa. E-mail: pnnomngongo@uj.ac.za

[b] Department of Science and Innovation-National Research Foundation South Africa, South Africa

[c] Research Chair Initiative (DSI-NRF SARChI) in Nanotechnology for Water, University of Johannesburg, Doornfontein, 2028, South Africa

[d] Institute for Nanotechnology and Water Sustainability, College of Science, Engineering and Technology, University of South Africa, Florida Science Campus, Roodepoort, 1710, South Africa

[e] School of Environmental Science and Engineering, Nanjing Tech University, Puzhu Nan Lu 30, Nanjing 211800, PR China

† Electronic supplementary information (ESI) available. See DOI: https://doi.org/10.1039/d5ra02767e

dizziness, headache, *etc.* Recent studies demonstrated that 30–40% of ACE released into the environment is not metabolized, and it is excreted through urination.[11] ACE is toxic to both terrestrial and aquatic organisms. The mechanism of action involves specific non-target effects on non-target organisms or target effects on non-target organisms. In addition, ACE could potentially destroy aquatic organisms by stimulating destabilization of lysosomal membrane and peroxidation of lipids in the digestive gland tissues of *Mercenaria*.[12] ACE can also influence cAMP-dependent cell antennae and actuate stress response in mussels.[13]

Other studies have shown that ACE has the potential to disrupt endocrine pathways by lowering testosterone levels in males.[14] While other organic pollutants can be degraded by direct photodegradation, hydrolysis and biodegradation, β-blockers, especially ACE, can transform through photolysis owing to its environmental half-life of over a year. However, if photolysis is performed under simulated sunlight, the half-lives of ACE and other β-blockers, can range from 16 to 630 h, which accounts for their continuing toxicity in the environment.[15] With rapid industrialization and the emergence of new diseases, it is expected that more ACE will be released into the environment. Therefore, there is a need to devise effective methods to sequester this refractory pollutant from the environment.

Various traditional techniques, including adsorption,[16] membrane filtration,[17] advanced oxidation processes (AOPs)[18] and biological methods,[19] have been proposed as successful techniques for the sequestration of pharmaceuticals from aquatic systems. Among these techniques, AOPs have stimulated huge interest from researchers worldwide due to their fascinating features, such as high photocatalytic efficiencies, high redox potentials, good reproducibility, simplicity and cost-effectiveness.[20,21] Compared to biological and physical treatment processes, AOPs are known for their environmentally friendliness and do not generate secondary pollution.[22] AOPs include four classical mechanisms, namely, Fenton oxidation,[23] ozonation,[24] photochemical oxidation[25] and persulfate activation.[26] These processes generate very reactive radicals (*i.e.*, the hydroxyl radical ($HO\cdot$), superoxide radical ($\cdot O_2^-$), sulfate radical ($SO_4^{\cdot -}$) and singlet oxygen ($^1O_2$)), which transform recalcitrant organic pollutants into the harmless inorganics H_2O and CO_2.[27]

The key to the use of AOPs is the selection of suitable heterostructured photocatalysts. Various heterogeneous catalysts have been employed in combination with various oxidants (H_2O_2, O_3, light, persulfates, *etc.*) to mineralise organic pollutants.[28–31] The main advantage of using heterogeneous catalysts is that they can be conveniently recovered from the solution by various means, unlike homogeneous catalysts.[29] Catalysts for AOPs should meet certain requirements such as chemical and physical stability, sustainability, environmental friendliness and high catalytic efficiency. In addition, these catalysts should have a narrow energy band gap to capture visible light.[32] Materials such as titanium oxide (TiO_2), among others, have been extensively applied as photocatalysts for the degradation of various degradable complexes and organic pollutants.[33–35] When the energy of the radiation matches or is above the energy band gap of a photocatalyst, the valence band (VB) electrons (e^-) are excited to the conduction band (CB), whilst the photogenerated holes (h^+) remain in the VB. Subsequently, redox half-reactions (reduction and oxidation) involving electrons and holes occur, respectively. However, most photocatalysts suffer from charge carrier (e^-/h^+) recombination, which causes poor photocatalytic efficacy.[36,37] Therefore, attention has shifted to hybrid materials with enhanced separation of photogenerated charge carriers.

Metal–organic frameworks (MOFs) are currently potential candidates in recognition of their intrinsic and fascinating surface properties.[38,39] These unique features provide MOFs with great applications in various fields, including catalysis, molecular recognition, gas storage and gas sensors.[39] MOFs have also been applied as photocatalysts for degrading a wide range of organic pollutants from environmental waters.[38,40] However, these framework-structured materials suffer major drawbacks, including poor usage of solar light and poor separation of photogenerated charge carriers.[41] To mitigate the disadvantages mentioned above, many researchers have coupled MOFs with semiconductors to form heterostructured materials, which can improve photocatalytic activity.[40] Amine-based MIL-101(Cr) exhibits fascinating features that render it a potential photocatalyst for wastewater remediation, including meso-sized cages, high surface area and structural flexibility.[42] Its 3D structure has been reported to be conducive to mass charge transfer.[43] The amine group on NH_2-MIL-101(Cr) is crucial in maximising the light absorption ability. The basic mechanism involves the transfer of N 2p electrons to the π^* orbitals of the terephthalic acid benzene ring to form a new highest occupied molecular orbital (HOMO), shifting the absorption edge towards higher wavelengths.[42] Furthermore, doping with amine increases the Fermi level closer to the CB, which encourages the electrons from the VB to transit to the CB. The latter will improve the conductivity and ultimately the photoelectrochemical properties. It is also worth noting that the ability of semiconductors to be more conductive relies on the availability of more electron donor atoms.[44]

Recent studies have revealed the efficacy of the 3D topology of MIL-101(Cr) in facilitating charge migration and ultimately promoting high photocatalytic activity towards the degradation of carbamazepine.[45] However, this material possesses a large energy band gap (2.65 eV) and weak electric fields between band edges, which reduce the photogeneration of charge carriers (e^-/h^+ pairs).[45] Magnetic nanoparticles (Fe_3O_4) possess a small energy band gap, which promotes visible light absorption. Furthermore, Fe_3O_4 nanoparticles have been considered to be suitable semiconductor materials due to their high thermal stability and eco-friendly features.[46] Therefore, coupling Fe_3O_4 nanoparticles with high-energy band gap semiconductors can improve the photoelectrochemical features of the hybridized material. Moreover, incorporating Fe_3O_4 particles facilitates the recovery of the composite using an external magnet.

In this study, Fe_3O_4 and amine-based MIL-101(Cr) were combined *via in situ* chemical co-precipitation to establish an efficient heterostructured Fe_3O_4@NH_2-MIL-101(Cr) photocatalyst, which exhibited synergistic effects. To our knowledge, this is the first report of Fe_3O_4@NH_2-MIL-101(Cr) as an adsorbent and a photocatalyst for the mineralization of acebutolol under ultraviolet irradiation. The possible photocatalytic mechanisms were evaluated using UV-Vis DRS, EIS and radical-trapping experiments. The main focus of this work was the assessment and comparison of six classical contribution processes towards the degradation of ACE. These contributions include adsorption only, UV only, H_2O_2 + UV, UV + photocatalysis, H_2O_2 + photocatalysis, and H_2O_2 + photocatalysis + UV. The use of the Fe_3O_4@NH_2-MIL-101(Cr) photocatalyst assisted in the generation of ROS, which were involved in the mineralization of ACE. The Fe_3O_4@NH_2-MIL-101(Cr) photocatalyst was chosen due to a few advantages: (I) The amine moiety provides additional adsorption sites with improved optical properties. (II) Chromium acts as the surface on which the transformation of the oxidants takes place. In addition, the Cr-based MOFs exhibit the best surface properties. (III) Lastly, Fe_3O_4 exhibits a strong electric field, which reduces the recombination of the photogenerated charge carriers in the Fe_3O_4@NH_2-MIL-101(Cr) nanocomposite. The nanocomposite material is environmentally friendly and can be obtained by facile synthesis methods, which is in line with a green chemistry approach. Therefore, this research project offers potential applications of efficient and environmentally friendly MOF composites for environmental wastewater remediation.

2. Experimental

2.1 Materials and chemicals

2-Aminoterephthalic acid (NH_2–H_2BDC), dimethylformamide (DMF), iron(II) chloride tetrahydrate ($FeCl_3\cdot 4H_2O$), hydrochloric acid (HCl, 37%), potassium chloride (KOH), iron(III) chloride hexahydrate ($FeCl_3\cdot 6H_2O$), chromium chloride nonahydrate ($Cr(NO_3)_3\cdot 9H_2O$), Nafion, ethanol, potassium chloride (KCl), acetonitrile (HPLC grade), sodium hydroxide (NaOH), ammonium solution (NH_4OH) (25%), acetone, and hydrogen peroxide (H_2O_2) were procured from Sigma Aldrich (USA). A stock solution of a β-blocker standard (ACE) was prepared and refrigerated at 2 °C. Ultrapure water generated with a Milli-Q system was used to dilute the standards.

2.2 Synthesis of Fe_3O_4 nanoparticles and amine-based MIL-101(Cr)

Synthesis of iron nanoparticles (Fe_3O_4) followed previous procedure reported by.[47] Synthesis of amine-based MIL-101(Cr) followed the procedure adopted by Mehrabadi and Faghihian.[48] Typically, 1.45 g NH_2–H_2BDC was combined with 3.19 g $Cr(NO_3)_3\cdot 9H_2O$ in a 100 mL beaker containing 60 mL of ultrapure water and 0.8 g NaOH. The resulting solution was allowed to mix through stirring for 30 min at 25 °C. The homogeneous solution was then transferred into a Teflon-based hydrothermal autoclave that was heated at 150 °C in an oven for 14 h. The heated mixture was cooled at 25 °C for over 6 h. The solid contents were collated *via* centrifugation. Thereafter, the contents were repeatedly purified with ethanol, DMF and ultrapure water, and the product was dried at 60 °C for 12 h in an oven.

2.3 Synthesis of the nanocomposite

Fabrication of the nanocomposite followed the typical chemical co-precipitation method adopted by Cai and co-workers.[49] Concisely, 2.02 g $FeCl_3\cdot 4H_2O$ and 4.04 g $FeCl_3\cdot 6H_2O$ were mixed in a 200 mL beaker containing 150 mL of ultrapure water. The solution was then added into a beaker containing 1 g Fe_3O_4@NH_2-MIL-101(Cr) and mixed for 45 min through stirring. During stirring, NH_4OH (25%) was added dropwise to the mixture until the pH reached 10. The mixture was allowed to stir for an additional 30 min at 25 °C until a black suspension was observed. The formed Fe_3O_4@NH_2-MIL-101(Cr) was collected using an external magnet and then cleaned successively with ultrapure water and acetone. The product was vacuum-dried at 50 °C for 14 h.

2.4 Instrumentation

The analytical techniques applied to characterize the materials as well as the chromatographic method are similar to those reported in our previous study.[50]

For photoelectrochemical properties: The optoelectronic properties were analysed using UV-vis diffuse reflectance spectra (DRS, JASCO V 670 instrument, Japan), and measurements were conducted at 200–1000 nm. The photoluminescence (PL) spectra were acquired using a fluorescence spectrophotometer (Hitachi F-7000). The electrochemical properties were measured with an Autolab PGSTAT204 electrochemical workstation (Netherlands) using 0.1 M potassium chloride (KCl) as an electrolytic solution. The working electrode was conductive 2.5 cm × 1.7 cm fluorine-doped titanium oxide (FTO). Ag/AgCl and platinum wire were used as the reference and counter electrodes, respectively. The photocatalytic experiments were conducted in a double-walled cell with UV lamp illumination (500 W, 200–400 nm) with an intensity of 920 mW cm^{-2}.

2.5 Photocatalytic experiments

Batch mode photocatalytic experiments were carried out in a double-walled reactor cell to evaluate the degradation of ACE. The photocatalytic system consisted of a UV lamp (500 W, 365 nm) with an intensity of 920 mW cm^{-2} positioned 15 cm above the reaction vessel. Briefly, 60 mg of the nanocomposite was placed in a 100 mL glass reactor containing 50 mL of a 10 mg L^{-1} solution of ACE. The pH of the solution was kept at 7, and the reaction was allowed to reach equilibrium in the dark through sonication. Subsequently, a 1 mL aliquot of the sample was analysed using HPLC-DAD. The procedure was repeated with the addition of 100 μL of H_2O_2. Afterwards, the solution was irradiated, and 1 mL was aliquoted, filtered and analysed using HPLC-DAD at a detection wavelength of 220 nm. Trapping experiments were conducted, and the significance of the adsorbent dosage and pH were evaluated. The pH adjustments were conducted using 0.2 NaOH/HCl. The pH was varied from 3 to 12 and the adsorbent dosage was varied from 10 to 70 mg.

The following formula was used to measure the amount of ACE degraded:

$$\%D = \frac{(C_0 - C_t)}{C_0} \times 100 \tag{1}$$

C_0 (mg L^{-1}) represents the initial sample concentration; C_t (mg L^{-1}) represents the sample concentration at time t.

2.6 Photoelectrochemical properties

The electrochemical properties of the materials were measured using an electrochemistry system constituting three electrodes coupled to an Autolab PGSTAT204 workstation (Netherlands) using 0.2 M KCl as a conducting solution. The working electrode was conductive fluorine-doped titanium oxide (FTO) glass (2.5 cm × 1.7 cm), which was fabricated as follows: 20 mg of a photocatalyst was immersed in 250 μL of a mixture containing 50 μL ethanol and 100 μL Nafion. The resulting solution was homogenized for about 20 min through sonication. The coated area on the FTO was about 1 cm^2, and the coated glass was oven-dried at 50 °C for 1 h. The reference and counter electrodes were Ag/AgCl and platinum wire, respectively. Nyquist and Bode plots were acquired using a frequency response analyser (FRA) with the following factors: voltage of 0.25 V, 100 mA to 100 nA current and frequency of 10 000 Hz. Mott–Schottky plots were acquired at the same frequency and were recorded from −2 to +2 V. The potentials obtained against Ag/AgCl were recalculated to the normal hydrogen electrode (NHE) scale using eqn (9).

3. Results and discussion

3.1 Characterisation section

3.1.1 Fourier transform infrared spectroscopy. FTIR spectroscopy was applied to identify the functional groups of the fabricated materials, and the FTIR spectra are shown in Fig. 1. The FTIR spectrum of Fe_3O_4 revealed an obvious intense band at 550 cm^{-1}, which corresponds to the vibrational stretching of Fe–O. This proved the successful synthesis of the Fe_3O_4 nanoparticles. The FTIR spectrum of NH_2-MIL-101(Cr) revealed observable peaks at 3085 and 3468 cm^{-1}, corresponding to the symmetric and asymmetric vibrational stretching of primary amine groups. In the same spectrum, the noticeable peaks seen at 1397 and 1624 cm^{-1} are ascribed to NH_2-MIL-101(Cr), which correspond to vibrational stretching of double carboxylate groups on terephthalic acid (H_2BDC).[51] Moreover, the salient peaks seen at 1019 and 750 cm^{-1} are ascribed to the vibrations of C–H in the benzene ring, which further substantiates the synthesis of NH_2-MIL-101(Cr).[52] This was further validated by the emergence of a noticeable peak at 666 cm^{-1}, which is associated with the vibrational band of Cr–O.[49] The FTIR spectrum of the nanocomposite revealed a strong band at 550 cm^{-1}. This band is related to the tensile vibrational stretching of Fe–O, confirming successful nanocomposite formation. Moreover, Cr–O and Fe–O were both observed in the nanocomposite, further confirming the successful synthesis of Fe_3O_4@NH_2-MIL-101(Cr) nanocomposite.

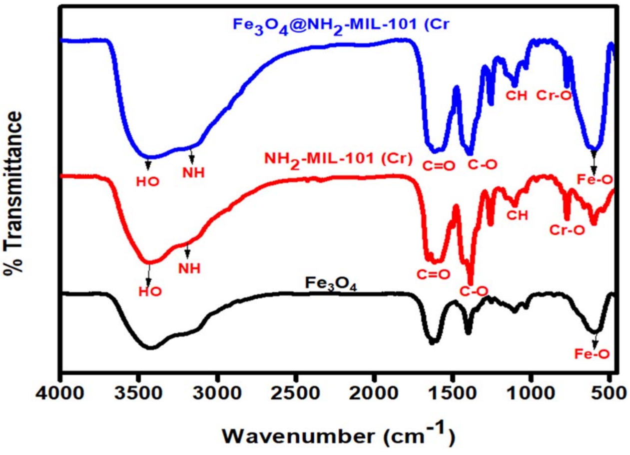

Fig. 1 FTIR spectra of the synthesized materials.

3.1.2 Brunauer–Emmett–Teller. The surface properties of the materials were estimated *via* Brunauer–Emmett–Teller analysis using the N_2 adsorption–desorption method. The findings are presented in Table 1, while the isotherm plots obtained at 77 K are shown in the ESI data (Fig. A.1).† As illustrated in Fig. A.1,† Fe_3O_4@NH_2-MIL-101(Cr) exhibited a type IV isotherm, indicating mesopores in the internal structure. The surface area, pore volume and pore size data are shown in Table 1. Upon doping NH_2-MIL-101(Cr) with Fe_3O_4, an observable drop in the pore volume and surface area was observed. This suggests that the Fe_3O_4 nanoparticles occupied some of the active sites on NH_2-MIL-101(Cr), resulting in compromised surface properties. However, the pore size increased, which was due to the strain within the pores caused by the introduction of Fe_3O_4 nanoparticles. Compared to the nanocomposite, pristine NH_2-MIL-101(Cr) exhibited higher pore volume and surface area, suggesting that this material could be used alone as a photocatalyst for the degradation of ACE. However, these properties had to be compromised by doping with Fe_3O_4 to avoid high recombination rates of the photogenerated charge carriers. The reduced surface area of the nanocomposite was satisfactory for the photocatalytic transformation of ACE. The high surface area suggests that there is an abundance of active sites on the surface, and the high pore volume indicates that there are abundant pores within Fe_3O_4@NH_2-MIL-101(Cr). This in turn indicates that the nanocomposite had all available sites to adsorb a high amount of ACE. In addition, the high surface area and pore volume promoted the adsorption of a high amount of oxidant (H_2O_2 and O_2). The more oxidant adsorbed on the photocatalyst surface, the more radicals are produced, which ultimately

Table 1 BET surface area, pore sizes and volumes of the synthesized materials

Material	Surface area (m^2 g^{-1})	Pore volume (cm^3 g^{-1})	Pore size (nm)
Fe_3O_4	190.6	0.28	1.96
NH_2-MIL-101(Cr)	2553.74	0.51	1.45
Fe_3O_4@NH_2-MIL-101(Cr)	1982.67	0.33	2.34

improves photocatalytic activity. Nonetheless, the compromised surface properties did not have an effect on the performance of the material towards the degradation of ACE.

3.1.3 X-ray diffraction spectroscopy. The structural state and composition of the synthesized materials were estimated using X-ray diffraction. The patterns are presented in Fig. 2. The pattern of Fe_3O_4 revealed crystalline peaks at 2θ angles of 31.3°, 36.1°, 42.9°, 54.1°, 58.2° and 62.9°, which correspond to the diffraction planes (220), (311), (400), (442), (511) and (440), respectively. This matches well with the diffraction peaks of Fe_3O_4 reported in the literature.[53,54] The XRD pattern of NH_2-MIL-101(Cr) revealed obvious crystalline peaks at 2θ angles of 5.7° and 15.2°, corresponding to the (101) and (220) diffraction planes, respectively. These peaks were in accordance with the typical crystalline peaks of NH_2-MIL-101(Cr) reported in previous studies.[55] The XRD pattern of the nanocomposite conserved the main diffraction peaks of Fe_3O_4 with a newly developed wide peak at 2θ angles between 2.1 and 28.7°. The conservation of the main diffraction peaks of Fe_3O_4 agrees well with the crystalline structure of Fe_3O_4 (JCPDS file 19-0629). This proved the successful synthesis of the heterostructures. The XRD pattern of NH_2-MIL-101(Cr) revealed slightly perceivable double peaks at 2θ angles of 24.7° and 42.5° which disappeared in the nanocomposite, indicating growth in crystal planes and a reduction in crystallite size.[56] The above-mentioned features were beneficial for the separation and transfer of the photogenerated charge carriers, which ultimately enhanced the photoelectrochemical features of the nanocomposite. The XRD pattern of the nanocomposite revealed that the XRD patterns of Fe_3O_4 predominated, suggesting that these nanoparticles were fairly disseminated on the external surface of NH_2-MIL-101(Cr). These claims were supported by the TEM image in Fig. 3(C).

3.1.4 Transmission electron microscopy. Transmission electron microscopy was employed to evaluate the internal structure of the synthesized materials. The findings are illustrated in Fig. 3. The TEM image of Fe_3O_4 (Fig. 3(A)) reveals well-distributed sphere-like particles, which are similar to those reported in the literature.[57] The TEM image of NH_2-MIL-101(Cr) (Fig. 3(B)) revealed octahedral-shaped structures that are similar to the ones reported in recent studies.[49] Fig. 3(C) shows the TEM image of the nanocomposite, revealing the distribution of Fe_3O_4 nanoparticles on the external surface of the nanocomposite, increasing surface roughness. A density of Fe_3O_4 agglomeration is observed at the octahedral edges of NH_2-MIL-101(Cr). The selected area electron diffraction (SAED) pattern of the nanocomposite is shown in Fig. 3(D). The SAED pattern resembles the diffraction patterns of Fe_3O_4,[58] indicating the successful incorporation of Fe_3O_4 nanoparticles on the surface of NH_2-MIL-101(Cr).

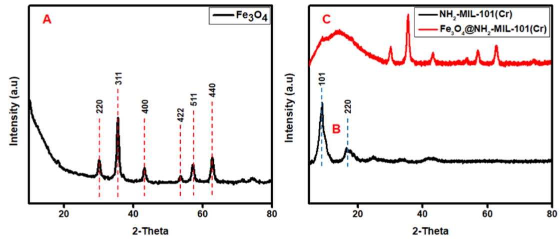

Fig. 2 XRD patterns of the synthesized materials.

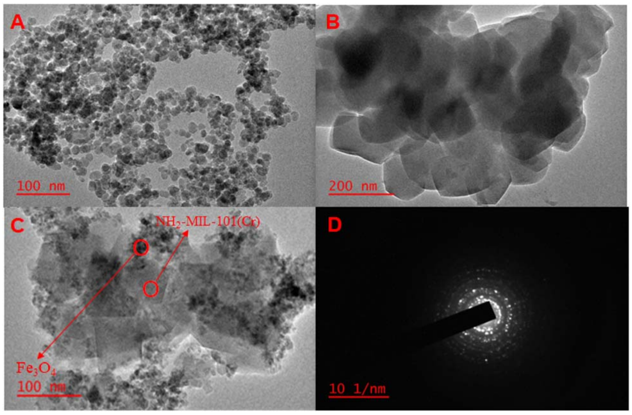

Fig. 3 TEM images of (A) Fe_3O_4 and (B) NH_2-MIL-101(Cr); (C) TEM image and (D) SAED of Fe_3O_4@NH_2-MIL-101(Cr).

3.1.5 Analysis of surface properties and chemistry of the nanocomposite (point of zero charge). The surface charge and chemistry of the nanocomposite were evaluated in terms of the point of zero charge (PZC) by applying the pH drift method. The results are depicted in Fig. A.2.† As observed, the PZC was seen at a pH of 8.3, indicating that the nanocomposite acquired positive and negative charges below and above pH 8.3.

3.2 UV-vis spectroscopy and photoluminescence analysis

3.2.1 Optoelectronic properties. Fig. 4(A) indicates the optoelectronic features of the synthesized materials obtained *via* UV-vis-DRS. An observable broad peak of NH_2-MIL-101(Cr) was seen at 600 nm and an intense absorption edge was seen at 390 nm; these are assigned to the d–d accepted transitions of Cr^{3+} and π–π transitions of the 2-aminoterephthalic acid ligand, respectively.[59] Furthermore, the observed broad peak resulted from the amine moiety on NH_2-MIL-101(Cr). However, the intensity of absorption edges was slightly reduced after nanocomposite formation, which could account for the intrinsic optical properties of the Fe_3O_4 nanoparticles and the obtained light brown colour of the nanocomposite.[60] The energy band gaps of the materials were obtained by conversion of the reflectance spectra values to Kubelka–Munk coordinates, and

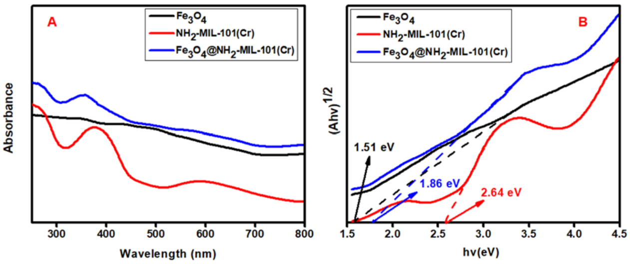

Fig. 4 UV-vis DRS (A) and Tauc plots (B) of the synthesized materials.

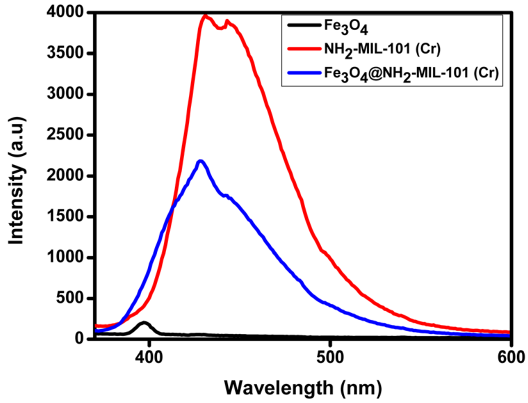

Fig. 5 Photoluminescence spectra of the synthesized materials.

then the Tauc plot was obtained as a function of $(Ah\nu) = vs.\ h\nu$ according to the equation below, and the results are shown in Fig. 4(B).

$$a(h\nu) = A(h\nu - E_g)^{1/2} \tag{2}$$

where ν, h, A, a and E_g (eV) are the photon frequency, Plank's constant ($6.62607015 \times 10^{-34}$ J Hz^{-1}), Tauc constant, absorption coefficient and energy band gap (eV), respectively.

The energy band gaps (E_g) obtained from the x-intercepts extrapolated from the tangent lines of the curves were estimated to be 1.51, 2.64 and 1.86 eV for Fe_3O_4, NH_2-MIL-101(Cr) and Fe_3O_4@NH_2-MIL-101(Cr), respectively. The E_g of the nanocomposite is lower than that of NH_2-MIL-101(Cr), suggesting the narrowing of the E_g after the incorporation of Fe_3O_4 nanoparticles. This aids in the rapid creation and subsequent segregation of photocatalytic charge carriers.

3.2.2 Photoluminescence. Photoluminescence (PL) measurements were applied to evaluate the separation rates of the photogenerated charge carriers, and the results are illustrated in Fig. 5. As shown in Fig. 5, the PL peak of the nanocomposite was remarkably reduced after the introduction of Fe_3O_4, which evidences that the synergistic effects existing between the pristine materials improved segregation of the photogenerated charge carriers and ultimately facilitated induced mass charge transfer on the interface.[61]

3.3 Contribution of pH and adsorbent dosage to the degradative process

To attain the best experimental outcomes for every analysis, optimisation of the parameters affecting the analytical response is necessary. Therefore, the effects of pH and adsorbent dosage were investigated, and the findings are presented in Fig. A.3 and A.4,† respectively. Acebutolol consists of two reactive sites, the amine moiety and the aromatic ring. The reactivity of the amine moiety is dependent on the pH, whilst that of the aromatic ring is not. As indicated in Fig. A.3,† the photocatalytic efficiency was low at pH 3 and 6, while it was greatly enhanced when the pH approached 9. Based on Fig. A.2,† the PZC of the photocatalyst was observed to pH 8.3, which suggests that the surface charge of the nanocomposite was positive below pH 8.3 and negative above pH 8.3.[61] At pH values below the PCZ, both Fe_3O_4@NH_2-MIL-101(Cr) and ACE had positive charges, which promoted electrostatic repulsion, and the latter resulted in reduced photocatalytic efficiency. However, Fe_3O_4@NH_2-MIL-101(Cr) possessed a negative charge when the pH exceeded 8.3, and electrostatic interactions were activated between the negative charges on the nanocomposite and positively charged ACE. The positive charges on the surface of ACE were still present until the pH exceeded 9.67, which is the pK_a of ACE. When the pH exceeded its pK_a (pH > 9.67), the surface of ACE acquired a negative charge, which then encouraged electrostatic repulsion, and the binding of ACE was affected. However, the photodegradation efficiency observed in Fig. A3† collapsed slightly when the pH reached 12, demonstrating additional mechanisms of interaction. Fig. A.4† illustrates the contribution of the adsorbent dosage to the degradation of ACE. As indicated, low degradation efficiency was attained when the adsorbent dosage was 10 mg, which could be ascribed to limited active sites on the external surface of the photocatalyst. Conversely, increased photodegradation efficiency was observed when the adsorbent dosage reached 70 mg due to the abundance of catalytic active sites on the photocatalyst.

3.4 Photocatalytic activity, kinetics and the effect of six classical processes on the degradation of ACE

The dark control experimental curves for the adsorption and subsequent photodegradation of ACE over various photocatalysts are illustrated in Fig. A.5.† These results show that the adsorption plateau was established after 60 min, and a negligible amount of ACE was removed using all the photocatalysts. In addition, 100 μL of hydrogen peroxide (H_2O_2) was added to evaluate its contribution to degradation efficiency.[45] Based on the results obtained, H_2O_2 exhibited a significant contribution to the photocatalytic activity of the photocatalysts. The photocatalytic activity of the nanocomposite was further assessed by degrading ACE under UV light illumination ($\lambda \leq 400$), and the

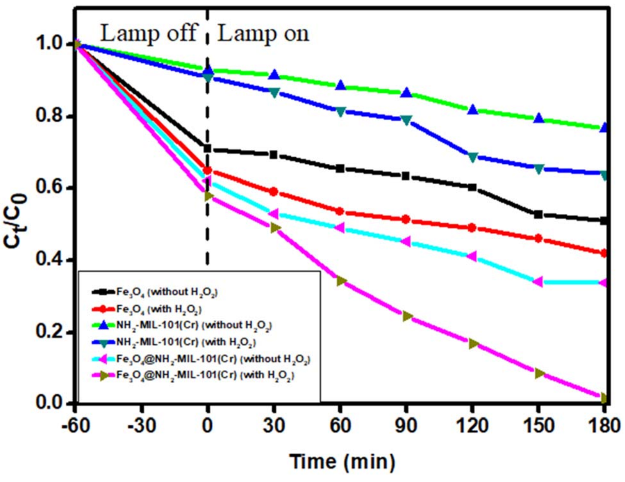

Fig. 6 Photodegradation efficiency over various photocatalysts with and without H_2O_2.

results are shown in Fig. 6. Photodegradation studies were also assessed in the absence and presence of H_2O_2 as an oxidant, and the results show that the presence of H_2O_2 had an observable impact on the photocatalytic activity of the prepared materials. This could be due to the availability of additional HO·, which was constantly formed *via* the self-decomposition of H_2O_2 in the presence of light[62]. However, Fe_3O_4 and NH_2-MIL-101(Cr) had significantly lower photocatalytic activity owing to the enhanced recombination rates of their charge carriers.[63] The magnetic nanoparticles also exhibited low recombination rates compared to NH_2-MIL-101(Cr), as supported by the PL results in Fig. 5. This was due to the strong electric fields between the band edges, which minimised the recombination rates of the charge carriers and enhanced optical properties.[64] The synergistic photochemical features of the two materials were integrated, and the photocatalytic performance of the nanocomposite was enormously enhanced, with the amount of ACE in the solution reaching lower concentrations after 180 min. The incorporation of Fe_3O_4 creates a heterostructured material that facilitates the segregation and transfer of photogenerated e^-/h^+ pairs, and the latter improves the photocatalytic activity.

To gain insights into the adsorption kinetics phenomena for the photodegradation of ACE, the rate constant (k) was obtained using the expression below, and the expression followed pseudo-first-order reaction kinetics.[45]

$$\ln\left(\frac{C_t}{C_0}\right) = -(kt) \tag{3}$$

where C_0 represents initial the concentration, C_t represents the concentration at time t, and k represents the rate constant.

Comparing the k values for all materials in the dark, the k value (0.01067 min^{-1}) for the nanocomposite (Fe_3O_4@NH_2-MIL-101(Cr)) was found to be greater than the k values for Fe_3O_4 (0.00664 min^{-1}) and NH_2-MIL-101(Cr) (0.00154). When exposed to UV light, the nanocomposite exhibited an increased k value (0.08791 min^{-1}) as did with Fe_3O_4 (0.01154 min^{-1}) and (NH_2-MIL-101(Cr)) (0.0098 min^{-1}), indicating that the photodegradation process played a significant role during the removal process (Fig. 7).

The effect of six classical processes on ACE degradation were assessed, and the findings are illustrated in Fig. A.6.† These include adsorption, UV only, H_2O_2 + UV, UV + photocatalyst, H_2O_2 + photocatalyst and H_2O_2 + UV + photocatalyst. β-Blockers are not easily degraded by either UV or visible light, and this was seen in the results when UV was the only possible catalytic process. When hydrogen peroxide was coupled with UV, very small amounts of ACE were degraded, which could be due to very small amounts of ROS produced by UV activation. Slight degradation occurred when either UV or H_2O_2 was coupled with Fe_3O_4@NH_2-MIL-101(Cr). However, when H_2O_2 + UV + photocatalyst were all coupled, the degradation efficiency improved greatly indicating that UV contributed significantly towards the breakdown of H_2O_2 to form ROS on the photocatalyst surface, which further mineralized ACE to CO_2 and H_2O. The results were supported by the obtained rate constant for H_2O_2 + UV + photocatalyst, which was high compared to the other processes, indicating improved kinetics and degradation efficiency.

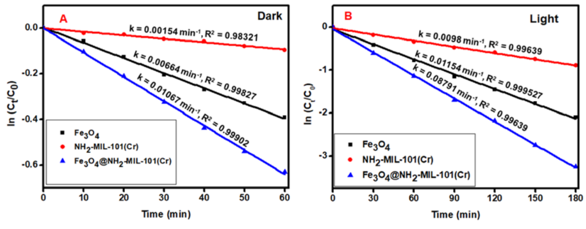

Fig. 7 Pseudo-first order kinetics of the nanocomposite for the degradation of ACE in the (A) dark and (B) under light illumination.

3.5 Reusability studies

The regenerability and reusability of the nanocomposite were assessed *via* a series of experiments. The spent photocatalyst was cleaned a few times with water and methanol and then dried for 7 h at 70 °C. Thereafter, the photocatalyst was reused in the next photodegradation process following the same procedure outlined in Section 2.5. The results are depicted in Fig. 8. In these results, it is salient that the photocatalyst could still maintain the optimum photocatalytic response after the second cycle, retaining over 80% degradation efficiency. However, the photocatalytic response was dramatically reduced after the third cycle, indicating that the photocatalyst could not be used more than three times for the degradation of ACE. This is due to the compromised stability of the nanocomposite in the presence of the provided light and the fact that the adsorption sites could not properly be emancipated during washing.[55] Furthermore, a more basic solution resulted in alkali corrosion, which could disintegrate the photocatalyst catalytic sites.[65] Nonetheless, the nanocomposite exhibited great photocatalytic efficiency and could potentially degrade a wide range of recalcitrant organic pollutants.

3.6 Trapping experiments

To evaluate the photocatalytic mechanism of ACE, trapping experiments for active radicals were conducted using *t*-butanol

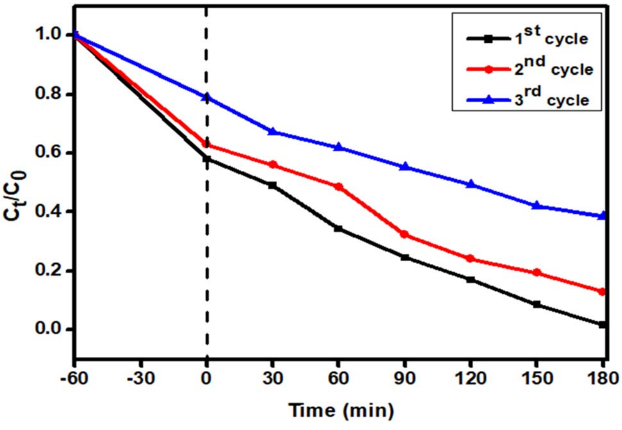

Fig. 8 Reusability studies for the degradation of ACE over the nanocomposite.

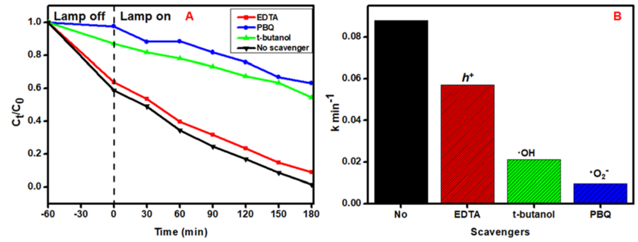

Fig. 9 The effect of (A) scavengers on the degradation of ACE and (B) the corresponding rate constants.

(1 mL), disodium ethylenediaminetetraacetate (EDTA, 1 mL) and 1,4-benzoquinone (PBQ, 1 mL). These were utilized as scavenging agents for hydroxyl radicals (HO·), holes (h^+) and superoxide radicals ($·O_2^-$), respectively. Fig. 9 (A) illustrates the effect of the radical scavengers on the photocatalytic efficacy of ACE. Notably, a slight inhibition in photocatalytic activity was observed when EDTA was added to the solution as a scavenger for h^+, suggesting that h^+ is not predominantly controlling the photocatalytic process. Conversely, moderate inhibition of HO· was observed when *t*-butanol was added, indicating that HO· moderately affects the photodegradation process. Theoretically, alcohols are scavengers for HO· radicals, meaning that ACE (which belongs to the alcohol family) had a considerable effect as a scavenger for HO· radicals.[66] Nonetheless, the constant self-decomposition of H_2O_2 in light produced more HO·, contributing to photocatalytic efficacy. However, the photocatalytic activity was greatly reduced when PBQ was added, illustrating that $·O_2^-$ is the ROS that contributes most to the degradation of ACE. Comparably, PBQ exhibited more inhibiting action than *t*-butanol, demonstrating that $·O_2^-$ contributed more towards the photocatalytic efficacy for ACE degradation over the hybridised Fe_3O_4@NH_2-MIL-101(Cr) nanocomposite. This was further proven by the dramatic decrease in rate constant when PBQ was added as a scavenger for $·O_2^-$ (Fig. 9(B)). The degradation process was conducted under mild-to-moderately basic conditions to prevent the formation of hydroperoxyl radicals ($·O_2H$) under acidic conditions ($pH \leq 4.6$) (eqn (7)) and radical oxide anions ($O·^-$) in a strongly basic medium ($pH \geq 11$) (eqn (5)), as these formed radicals are not effective in mineralising most organic pollutants.[67] The equations are as follows:

$$h^+ + H_2O \rightarrow ·OH + H^+,\ E^\circ_{(NHE)}\ (·OH, H^+/H_2O) = 2.38\ V \quad (4)$$

$$·OH + HO^- \rightarrow H_2O + O·^-,\ pK_a = 11.8 \quad (5)$$

$$e^- + O_2 \rightarrow ·O_2^-,\ E^\circ_{(NHE)}\ (O_2/\ ·O_2^-) = -0.33\ V \quad (6)$$

$$·O_2^- + H^+ \rightarrow ·O_2H,\ pK_a = 4.9 \quad (7)$$

3.7 Photoelectrochemical properties and proposed degradation mechanism

Electrochemical impedance spectroscopy (EIS) was employed to further understand the interfacial charge separation and migration and the results are depicted as Nyquist plots in Fig. 10(A). The electrical circuits of the materials obtained from the fitted EIS data are shown in Fig. A.8 in the ESI.† The charge transfer resistance (R_{ct}) was determined *via* the magnitude of the semicircular diameter. The results revealed that the NH_2-MIL-101(Cr) semicircle was larger, implying high transfer resistance and low conductivity. Upon the incorporation of Fe_3O_4, the semicircle diameter was reduced significantly, indicating a smaller R_{ct} (Table 2), better conductivity and an improved charge separation capability. The solution resistance (R_s) was obtained as a non-null intercept at the *x*-axis on the Nyquist graph; the results are shown in Table 2. The improved optoelectronic features of the nanocomposite were complemented by the fascinating semiconducting feature of the Fe_3O_4 nanoparticles, and these results correspond with the PL data in Section 3.2.2. The results acquired showed that the formed Fe_3O_4@NH_2-MIL-101(Cr) heterojunction could allow for fast segregation and transfer of photogenerated charge carriers at the interfacial region of the nanocomposite.

Bode plots were obtained to determine the lifespan of a photoexcited electron, and the findings are depicted in Fig. 10(B). The maximum peak angular frequencies are also shown on the plots. All materials exhibited phase frequencies, which indicates their ability to photogenerate holes (h^+) and excited electrons (e^-). The following equation was used to estimate the lifespan of an excited electron:

$$\tau_e = \frac{1}{2\pi f_{max}} \quad (8)$$

where τ_e (ms) represents the lifespan of the photoexcited electron and f_{max} (Hz) is the phase frequency.

The τ_e values for all materials are shown in Table 2, and the τ_e increased in the following manner: Fe_3O_4 > Fe_3O_4@NH_2-MIL-101(Cr) > NH_2-MIL-101(Cr). The formed heterojunction combined the optical synergistic merits of Fe_3O_4 and NH_2-MIL-101(Cr), and the latter resulted in an increased τ_e, which signifies the effective segregation and transfer of the photogenerated charge carriers.[68] However, the τ_e value for Fe_3O_4 was still higher than that of the nanocomposite, and these data correspond with the findings reported previously by Xiao and co-workers.[69] Nonetheless, the heterojunction exhibited enhanced photoinduction and prolonged excited states compared to the parent NH_2-MIL-101(Cr), which are necessary for generating charges and their ultimate separation. Overall,

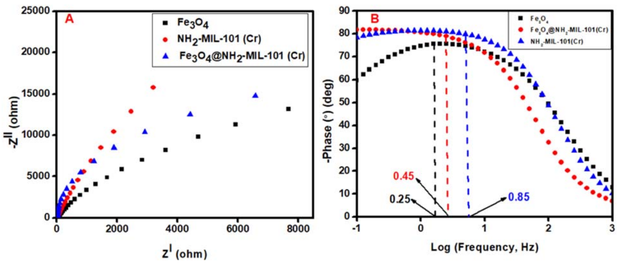

Fig. 10 Nyquist plots (A) and Bode phase plots (B) of the synthesized materials.

Table 2 Photoexcited electron lifespan values (τ_e) for the synthesised materials

Material	τ_e (ms)	R_s (Ω)	R_{ct} (Ω)
Fe_3O_4	8.95	26.67	25.21
NH_2-MIL-101(Cr)	2.25	31.77	260.42
Fe_3O_4@NH_2-MIL101(Cr)	5.65	21.1	93.1

the reduced E_g of the nanocomposite enabled maximum absorption of UV light and subsequent fast excitation of electrons from the VB to the CB. The photoluminescence results also indicated reduced recombination of charge carriers, which was supported by the increased τ_e and reduced R_{ct} (Table 2). The increased τ_e and reduced R_{ct} indicate that electrons had an extended residence time at the excited state and were ultimately able to migrate through an interface due to the reduced interface R_{ct}. The transferred electron was then able to activate the oxidants to generate radicals, which were used to destroy ACE.

Mott–Schottky plots were prepared to obtain more insight into the band structures of NH_2-MIL-101(Cr) and Fe_3O_4, and the findings are presented in Fig. A.7.†[70] The obtained slopes for both graphs were positive, indicating *n*-type semiconductor behavior for both NH_2-MIL-101(Cr) and Fe_3O_4.[60,63] The flat band potential (E_{fb}) of *n*-type semiconductors is equivalent to the CB, *i.e.*, $E_{fb} \approx$ CB. However, the CB was 0.2 V, which was slightly more negative than the E_{fb}.[71] After extrapolation, the E_{fb} was estimated to be −0.32 and −0.92 V *vs.* Ag/AgCl for Fe_3O_4 and NH_2-MIL-101(Cr), respectively. Calculations were made, and the potentials against NHE were obtained to be 0.077 and −0.523 V *vs.* NHE, respectively, using eqn (9).

$$E_{NHE} = E_{Ag/AgCl} + 0.197\ \mathrm{V} \tag{9}$$

The valence band potentials (VB) were also obtained using eqn (10) as 2.117 eV for Fe_3O_4 and 1.587 eV for NH_2-MIL-101(Cr).

$$E_{VB} = E_{CB} \tag{10}$$

The possible transfer mechanism of the photogenerated charge carriers is depicted in Fig. 11. After irradiation, the VB electrons of both materials are promoted to the CB *via* excitation. Charge transfer involves two probable mechanisms, which are the traditional type I and Z-scheme mechanisms. In the type I mechanism, the E_g of one semiconductor lies between the E_g of another semiconductor, as presented in Fig. 11(A).[72] Furthermore, the photogenerated electrons in the CB band of the NH_2-MIL-101(Cr) transit to the CB of Fe_3O_4 owing to the significantly more negative CB potential of NH_2-MIL-101(Cr). Moreover, the migration of holes followed a similar direction. The electrons in the CB of Fe_3O_4 have a more positive potential than $O_2/\cdot O_2^-$ (−0.33), which will make it impossible for the reduction process to be initiated.[73] Scavenging experiments indicated that $\cdot O_2^-$ radicals were the dominant reactive species. Therefore, the formed heterojunction followed the direct Z-scheme. In a Z-scheme heterojunction (Fig. 11(B)), the electrons in the CB of Fe_3O_4 recombine with VB holes of NH_2-MIL-101(Cr), maintaining the reducing ability of electrons in the CB of NH_2-MIL-101(Cr). Electrons in the CB of NH_2-MIL-101(Cr) can reduce O_2, forming $\cdot O_2^-$. This occurs because the CB of NH_2-MIL-101(Cr) bears greater negative potential compared to $E^{\ominus}$ $(O_2/\cdot O_2^-) = -0.33$.[56] The holes in the VB of Fe_3O_4 could not oxidise OH^- or H_2O due to VB bearing a less positive potential (1.587 V) than $H_2O/HO\cdot$ (2.40 V) and $OH^-/\cdot OH$ (1.98 V).[60] This trend agrees with the results obtained in this work. Hydrogen peroxide was added to contribute to the generation of more $HO\cdot$ according to eqn (11)–(13). However, eqn (13) indicates that H_2O_2 sacrifices $\cdot O_2^-$ to generate more $HO\cdot$. According to the scavenging experiments, $\cdot O_2^-$ was the main reactive species, which contradicts eqn (13). The lifespan of an electron for the nanocomposite was estimated to be 5.65 ms, which indicated that an electron had sufficient time to trap H_2O_2 from scavenging $\cdot O_2^-$.[45] Therefore, $\cdot O_2^-$ remained active for the degradation of ACE.

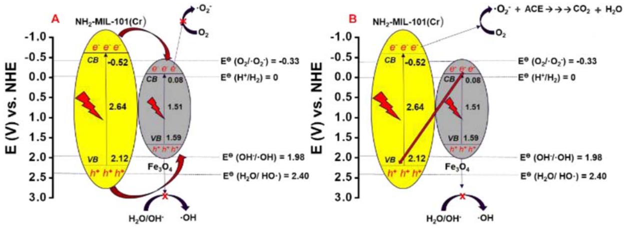

Fig. 11 Schematic depiction of the two photocatalytic degradation mechanisms (type I (A) and Z-scheme (B) heterojunctions) of ACE over Fe_3O_4@NH_2-MIL-101(Cr).

$$H_2O_2 + e^- \rightarrow OH^- + HO\cdot \tag{11}$$

$$H_2O_2 + h\nu \rightarrow 2\ HO\cdot \tag{12}$$

$$H_2O_2 + \cdot O_2^- \rightarrow OH^- + HO\cdot + O_2 \tag{13}$$

From the mechanism of electron flow, it can be concluded that the formed heterojunction follows the Z-scheme. The Z-scheme mechanism entails the movement of the photogenerated electrons from the CB of Fe_3O_4 through the interfacial structure to recombine with the VB holes of NH_2-MIL-101(Cr). This retains the reducing ability of electrons in the CB of NH_2-MIL-101(Cr). This mechanism further allows for better segregation of the photogenerated charge carriers and ultimately improves the reduction/oxidation capability of the hybrid surface for the effective degradation of ACT.

3.8 Comparison of the photocatalytic efficiency of the current photocatalyst with previously reported photocatalysts in the degradative removal of β-blockers

To evaluate the photocatalytic performance of the employed photocatalyst, comparison studies were conducted, and the results are shown in Table 3. The comparison was based on applying various photocatalysts towards the degradation of β-blockers. The most commonly and extensively used β-blockers

Table 3 Comparison of the current photocatalyst with other photocatalysts applied in the photodegradation of β-blockers[a]

Photocatalyst	Analyte(s)	Photocatalyst dosage (g)	Photodegradation time (min)	Photocatalytic efficiency (%)	Ref.
TiO_2/zeolite	MET	0.2	240	95	76
TiO_2	MET	0.5	125	98	87
Degussa P25	ACE, PRO	0.29	240	75–92	88
Degussa P25	ATE, MET, PRO	0.3	240	94.4–96.7	89
Fe(II)-citrate complex	PRO	—	37	50	90
H_2TF_5PP	MET	0.05	720	90	91
TiO_2	ACE	1	225	95	92
$n$$TiO_2$@$SnO_2$@Mn(5AB-HQ)	MET	0.1	10	98.6	93
Sodium nitrate	ATE	0.02	240	72	94
T-coated MAC	MET	—	180	98	95
GO-TiO_2	ATE	0.23	60	72	96
Biochar-TiO_2	MET, PRO	0.35	60	60–70	97
Fe_3O_4@NH_2-MIL-101(Cr)	ACE	0.07	180	98.3	This work

[a] TiO_2: Titanium oxide; Degussa P25: Commercial TiO_2 nanopowder Aeroxide® P25 (obtained from Evonik Degussa); T-coated MAC- Titania coated magnetic activated carbon. –: No specific adsorbent dosage; GO-TiO_2: Graphene oxide doped-titanium oxide; H_2TF_5PP: 5,10,15,20-tetrakis(pentafluorophenyl) porphyrin; $n$$TiO_2$@$SnO_2$@Mn(5AB-HQ): metal–organic frameworks/nano titanium oxide coated tin dioxide.

include atenolol (ATE), metoprolol (MET) and propranolol (PRO).[74] These β-blockers are highly detected in the environment, and their adverse effects are alarming.[75,76] Therefore, many researchers have primarily focused on eliminating these recalcitrant pollutants from the environment.[77] However, the fate, ubiquity and toxicity of other β-blockers, including ACE, cannot be avoided. Therefore, the current work focuses on the degradation of the β-blocker ACE, a representative model analyte for other β-blockers. This was done due to their structural similarities and inherent physicochemical properties. In addition, β-blockers have a similar main mechanism of degradation which involves the cleavage of side chains containing chiral carbon followed by hydroxylation.[78]

Moreover, reports documenting these compounds' degradation using traditional or advanced materials are scarce. Most of the studies reporting their degradation have employed commercial TiO_2 nanopowders as photocatalysts, and it is known that TiO_2 photocatalysts are expensive and possess low surface area and high energy band gaps, which hampers their applicability in wastewater remediation systems.[77–81] In the literature, a considerable number of research papers reporting the degradation of β-blockers have been documented using AOPs that are not conducted by the photocatalysts.[77,82–85] The photocatalytic systems involving the generation of these radicals are quite expensive and require special laboratory setups.[86] However, the current work employed an environmentally friendly and cheap photocatalyst for the destruction of ACE. The results presented in Table 3 suggest that the current photocatalyst exhibits efficient degradation efficiency and could potentially be used to completely eliminate various organic pollutants in the environment.

4. Conclusion

Chemical co-precipitation was used to successfully synthesise the Fe_3O_4@NH_2-MIL-101(Cr) hybrid. The nanocomposite revealed great photocatalytic performance for the efficient degradation of ACE under UV exposure. The mechanism of electron flow indicated that the hybrid followed the Z-scheme mechanism suggested by the UV-vis DRS, radical scavenging results, band edge position experimental analysis and Mott–Schottky analysis. The great photocatalytic performance offered by the nanocomposite was ascribed to its ability to form a Z-scheme heterojunction, which then improved the interfacial charge separation and transfer, as shown in the EIS results. The nanocomposite further exhibited great efficacy in the degradation of ACE. Furthermore, the hybrid displayed considerably acceptable reusability, as it was used at least three times, retaining more than 60% photocatalytic efficiency. This suggested that the nanocomposite could be reliably used to degrade a wide range of organic pollutants under UV illumination. The current photocatalyst demonstrated remarkable photocatalytic activity towards the degradation of ACE under UV illumination. However, UV light is toxic and not readily available. Future efforts will be to enhance visible light absorption for the degradation of a wide range of other pharmaceuticals.

Data availability

Kindly note that the data associated with the preparation of this manuscript is available upon request.

Author contributions

Waleng NJ: Conceptualization, data curation, methodology, visualization, investigation, writing original draft, formal analysis, funding acquisition, validation; Mundonde TS: Formal analysis, review and editing, validation; Mpupa A: Methodology, software, formal analysis, investigation, review and editing; Moremedi T: Review and editing, formal analysis, validation; Zhang Y: Validation, formal analysis, review and editing, supervision; Nomngongo PN: supervision, resources, review and editing, formal analysis, investigation, project administration, funding acquisition.

Conflicts of interest

None.

Acknowledgements

The authors are also grateful for the financial assistance provided by Department of Science and Innovation-National Research Foundation-South African Research Chair Initiative (DSI-NRF SARChI) programme, grant number 91230 and National Research Foundation (NRF, South Africa, grant no: 121638). The authors are grateful to the University of Johannesburg (Chemical Sciences department) for providing us with their laboratory facilities for conducting our experiments. The gratitude is further extended to Mrs Orienda Sebabi Molahlegi and Mr Siyasanga Mpelane for their assistance in characterisation techniques.

References

1 N. Morin-Crini, *et al.*, Worldwide cases of water pollution by emerging contaminants: a review, *Environ. Chem. Lett.*, 2022, **20**(4), 2311–2338.
2 N. J. Waleng and P. N. Nomngongo, Occurrence of pharmaceuticals in the environmental waters: African and Asian perspectives, *Environ. Chem. Ecotoxicol.*, 2022, **4**, 50–66.
3 S. Bayen, H. Zhang, M. M. Desai, S. K. Ooi and B. C. Kelly, Occurrence and distribution of pharmaceutically active and endocrine disrupting compounds in Singapore's marine environment: Influence of hydrodynamics and physical–chemical properties, *Environ. Pollut.*, 2013, **182**, 1–8, DOI: **10.1016/j.envpol.2013.06.028**.
4 L. M. Madikizela, *et al.*, Pharmaceuticals and their metabolites in the marine environment: Sources, analytical methods and occurrence, *Trends Environ. Anal. Chem.*, 2020, **28**, e00104, DOI: **10.1016/j.teac.2020.e00104**.
5 G.-G. Ying, J.-L. Zhao, L.-J. Zhou and S. Liu, Fate and occurrence of pharmaceuticals in the aquatic environment (surface water and sediment), *Compr. Anal. Chem.*, 2013, **62**, 453–557.
6 C. Mejias, J. Martin, J. L. Santos, I. Aparicio and E. Alonso, Occurrence of pharmaceuticals and their metabolites in sewage sludge and soil: A review on their distribution and environmental risk assessment, *Trends Environ. Anal. Chem.*, 2021, **30**, e00125.
7 X. Yu, F. Yu, Z. Li and J. Zhan, Occurrence, distribution, and ecological risk assessment of pharmaceuticals and personal care products in the surface water of the middle and lower reaches of the Yellow River (Henan section), *J. Hazard. Mater.*, 2023, **443**, 130369.
8 E. Vulliet, C. Cren-Olivé and M.-F. Grenier-Loustalot, Occurrence of pharmaceuticals and hormones in drinking water treated from surface waters, *Environ. Chem. Lett.*, 2011, **9**(1), 103–114.
9 L. Jiang, *et al.*, Pharmaceuticals and personal care products (PPCPs) in the aquatic environment: Biotoxicity, determination and electrochemical treatment, *J. Cleaner Prod.*, 2023, 135923.
10 A. S. Adeleye, *et al.*, Abundance, fate, and effects of pharmaceuticals and personal care products in aquatic environments, *J. Hazard. Mater.*, 2022, **424**, 127284.
11 U. Bussy, V. Ferchaud-Roucher, I. Tea, M. Krempf, V. Silvestre and M. Boujtita, Electrochemical oxidation behavior of Acebutolol and identification of intermediate species by liquid chromatography and mass spectrometry, *Electrochim. Acta*, 2012, **69**, 351–357.
12 B. Khan, R. M. Burgess, S. A. Fogg, M. G. Cantwell, D. R. Katz and K. T. Ho, Cellular responses to *in vitro* exposures to β-blocking pharmaceuticals in hard clams and Eastern oysters, *Chemosphere*, 2018, **211**, 360–370.
13 S. Franzellitti, S. Buratti, P. Valbonesi, A. Capuzzo and E. Fabbri, The β-blocker propranolol affects cAMP-dependent signaling and induces the stress response in Mediterranean mussels, Mytilus galloprovincialis, *Aquat. Toxicol.*, 2011, **101**(2), 299–308.
14 N. J. Waleng and P. N. Nomngongo, Occurrence of pharmaceuticals in the environmental waters: African and Asian perspectives, *Environ. Chem. Ecotoxicol.*, 2022, **4**, 50–66.
15 Z. Ye, *et al.*, Photodegradation of acebutolol in natural waters: Important roles of carbonate radical and hydroxyl radical, *Chemosphere*, 2022, **287**, 132318, DOI: **10.1016/j.chemosphere.2021.132318**.
16 J. R. de Andrade, M. F. Oliveira, M. G. C. da Silva and M. G. A. Vieira, Adsorption of pharmaceuticals from water and wastewater using nonconventional low-cost materials: a review, *Ind. Eng. Chem. Res.*, 2018, **57**(9), 3103–3127.
17 P. Alfonso-Muniozguren, E. A. Serna-Galvis, M. Bussemaker, R. A. Torres-Palma and J. Lee, A review on pharmaceuticals removal from waters by single and combined biological, membrane filtration and ultrasound systems, *Ultrason. Sonochem.*, 2021, **76**, 105656.
18 D. Kanakaraju, B. D. Glass and M. Oelgemöller, Advanced oxidation process-mediated removal of pharmaceuticals from water: A review, *J. Environ. Manage.*, 2018, **219**, 189–207, DOI: **10.1016/j.jenvman.2018.04.103**.
19 M. Zupanc, *et al.*, Removal of pharmaceuticals from wastewater by biological processes, hydrodynamic cavitation and UV treatment, *Ultrason. Sonochem.*, 2013, **20**(4), 1104–1112.
20 I. M. D. Gonzaga, C. V. S. Almeida and L. H. Mascaro, A Critical Review of Photo-Based Advanced Oxidation Processes to Pharmaceutical Degradation, *Catalysts*, 2023, **13**(2), 221.
21 I. Michael, Z. Frontistis and D. Fatta-Kassinos, Removal of pharmaceuticals from environmentally relevant matrices by advanced oxidation processes (AOPs), *Compr. Anal. Chem.*, 2013, **62**, 345–407.
22 J. Tuerk, B. Sayder, A. Boergers, H. Vitz, T. K. Kiffmeyer and S. Kabasci, Efficiency, costs and benefits of AOPs for removal of pharmaceuticals from the water cycle, *Water Sci. Technol.*, 2010, **61**(4), 985–993.

23 E. M. Jiménez-Bambague, *et al.*, Photo-Fenton and Electro-Fenton Performance for the Removal of Pharmaceutical Compounds in Real Urban Wastewater, *Electrochim. Acta*, 2023, 141905.

24 E. Issaka, J. N.-O. Amu-Darko, S. Yakubu, F. O. Fapohunda, N. Ali and M. Bilal, Advanced catalytic ozonation for degradation of pharmaceutical pollutants–A review, *Chemosphere*, 2022, **289**, 133208.

25 A. H. Asif, *et al.*, Graphitic carbon nitride engineered α-Fe2O3/rGO heterostructure for visible-light-driven photochemical oxidation of sulfamethoxazole, *Chem. Eng. J.*, 2023, **451**, 138630.

26 Z. Kang, *et al.*, A review on application of biochar in the removal of pharmaceutical pollutants through adsorption and persulfate-based AOPs, *Sustainability*, 2022, **14**(16), 10128.

27 J. Jiao, *et al.*, Removal of Pharmaceuticals and Personal Care Products (PPCPs) by Free Radicals in Advanced Oxidation Processes, *Materials*, 2022, **15**(22), 8152.

28 Y. He, *et al.*, Co-doped 3D petal-like ZnIn2S4/GaN heterostructures for efficient removal of chlortetracycline residue from real pharmaceutical wastewater, *Chem. Eng. J.*, 2022, **446**, 137355.

29 A. Garg, S. Basu, N. P. Shetti and K. R. Reddy, 2D materials and its heterostructured photocatalysts: Synthesis, properties, functionalization and applications in environmental remediation, *J. Environ. Chem. Eng.*, 2021, **9**(6), 106408.

30 E. H. Rdewi, K. K. Abbas and A. M. H. AbdulkadhimAl-Ghaban, Removal pharmaceutical carbamazepine from wastewater using ZnO-TiO2-MXene heterostructural nanophotocatalyst under solar light irradiation, *Mater. Today: Proc.*, 2022, **60**, 1702–1711.

31 M. Akkari, P. Aranda, C. Belver, J. Bedia, A. B. H. Amara and E. Ruiz-Hitzky, Reprint of ZnO/sepiolite heterostructured materials for solar photocatalytic degradation of pharmaceuticals in wastewater, *Appl. Clay Sci.*, 2018, **160**, 3–8.

32 N. Madkhali, *et al.*, Recent update on photocatalytic degradation of pollutants in waste water using TiO2-based heterostructured materials, *Results Eng.*, 2023, 100920.

33 E. M. Van Wieren, M. D. Seymour and J. W. Peterson, Interaction of the fluoroquinolone antibiotic, ofloxacin, with titanium oxide nanoparticles in water: Adsorption and breakdown, *Sci. Total Environ.*, 2012, **441**, 1–9.

34 M. O. Miranda, *et al.*, Photocatalytic degradation of ibuprofen using titanium oxide: insights into the mechanism and preferential attack of radicals, *RSC Adv.*, 2021, **11**(44), 27720–27733.

35 W. Z. Khan, I. Najeeb, S. Ishtiaque and S. Jabeen, Photodegradation of real pharmaceutical wastewater with titanium dioxide, zinc oxide, and hydrogen peroxide during UV, *IOSR-JEN*, 2016, **6**(7), 36–46.

36 M. Sharma, A. Yadav, M. K. Mandal and K. K. Dubey, TiO2 based photocatalysis: a valuable approach for the removal of pharmaceuticals from aquatic environment, *Int. J. Environ. Sci. Technol.*, 2023, **20**(4), 4569–4584.

37 D. Zhou, Y.-Y. Wang, F.-R. Wang, J.-K. Liu and X.-M. Zhang, Design and application of Ag3PO4@ Ag4V2O7 Z-scheme photocatalysts with a micro-nano tube-cluster structure for the co-degradation of nitrate and ammonia in wastewater, *Ind. Eng. Chem. Res.*, 2019, **58**(39), 18027–18035.

38 S. Gautam, *et al.*, Metal oxides and metal organic frameworks for the photocatalytic degradation: A review, *J. Environ. Chem. Eng.*, 2020, **8**(3), 103726.

39 C. P. Raptopoulou, Metal-organic frameworks: Synthetic methods and potential applications, *Materials*, 2021, **14**(2), 310.

40 Z. U. Zango, *et al.*, A critical review on metal-organic frameworks and their composites as advanced materials for adsorption and photocatalytic degradation of emerging organic pollutants from wastewater, *Polymers*, 2020, **12**(11), 2648.

41 T. Xia, Y. Lin, W. Li and M. Ju, Photocatalytic degradation of organic pollutants by MOFs based materials: A review, *Chin. Chem. Lett.*, 2021, **32**(10), 2975–2984.

42 X. Li, Y. Pi, Q. Xia, Z. Li and J. Xiao, TiO2 encapsulated in Salicylaldehyde-NH2-MIL-101(Cr) for enhanced visible light-driven photodegradation of MB, *Appl. Catal., B*, 2016, **191**, 192–201.

43 M. Wu, *et al.*, Construction of 3D porous BiOBr/MIL-101(Cr) Z-scheme heterostructure for boosted photocatalytic degradation of tetracycline hydrochloride, *Sep. Purif. Technol.*, 2023, **307**, 122744.

44 A. Kongkanand and P. V Kamat, Electron Storage in Single Wall Carbon Nanotubes. Fermi Level Equilibration in Semiconductor–SWCNT Suspensions, *ACS Nano*, 2007, **1**(1), 13–21, DOI: 10.1021/nn700036f.

45 Q. Huo, *et al.*, Preparation of a direct Z-scheme α-Fe2O3/MIL-101(Cr) hybrid for degradation of carbamazepine under visible light irradiation, *Appl. Catal., B*, 2019, **255**, 117751.

46 M. Ul-Islam, *et al.*, Current advancements of magnetic nanoparticles in adsorption and degradation of organic pollutants, *Environ. Sci. Pollut. Res.*, 2017, **24**, 12713–12722.

47 N. J. Waleng, S. K. Selahle, A. Mpupa and P. N. Nomngongo, Development of dispersive solid-phase microextraction coupled with high-pressure liquid chromatography for the preconcentration and determination of the selected neonicotinoid insecticides, *J. Anal. Sci. Technol.*, 2022, **13**(1), 1–15.

48 Z. Mehrabadi and H. Faghihian, Comparative photocatalytic performance of TiO2 supported on clinoptilolite and TiO2/Salicylaldehyde-NH2-MIL-101(Cr) for degradation of pharmaceutical pollutant atenolol under UV and visible irradiations, *J. Photochem. Photobiol., A*, 2018, **356**, 102–111.

49 Y. Cai, *et al.*, Efficient capture of ReO4− on magnetic amine-functionalized MIL-101(Cr): Revealing from selectivity to mechanism, *Sci. Total Environ.*, 2021, **771**, 144840, DOI: 10.1016/j.scitotenv.2020.144840.

50 N. J. Waleng, S. K. Selahle, A. Mpupa, Y. Zhang and P. N. Nomngongo, Development of Magnetic Solid Phase Micro-Extraction (MSPE) Method for the Extraction and

Preconcentration of the Selected β-Blockers in the Environmental Wastewaters, *Chem. Afr.*, 2024, 1–17.

51 M. Shafiei, M. S. Alivand, A. Rashidi, A. Samimi and D. Mohebbi-Kalhori, Synthesis and adsorption performance of a modified micro-mesoporous MIL-101(Cr) for VOCs removal at ambient conditions, *Chem. Eng. J.*, 2018, **341**, 164–174.

52 M. Hartmann and M. Fischer, Amino-functionalized basic catalysts with MIL-101 structure, *Microporous Mesoporous Mater.*, 2012, **164**, 38–43.

53 N. Karami, *et al.*, Green synthesis of sustainable magnetic nanoparticles Fe3O4 and Fe3O4-chitosan derived from Prosopis farcta biomass extract and their performance in the sorption of lead(II), *Int. J. Biol. Macromol.*, 2024, **254**, 127663, DOI: 10.1016/j.ijbiomac.2023.127663.

54 X.-Y. Li, W.-Q. Ding, P. Liu, L. Xu, M.-L. Fu and B. Yuan, Magnetic Fe3O4/MIL-101 composite as a robust adsorbent for removal of p-arsanilic acid and roxarsenic in the aqueous solution, *Colloids Surf., A*, 2023, **662**, 131014.

55 S. Walia, M. Kaur and S. K. Kansal, Adsorptive removal of 2,4-dinitrophenol from aqueous phase using amine functionalized metal organic framework (NH2-MIL-101(Cr)), *Mater. Chem. Phys.*, 2022, **289**, 126493, DOI: 10.1016/j.matchemphys.2022.126493.

56 H. Shi, C. Li, L. Wang, W. Wang, J. Bian and X. Meng, Efficient photocatalytic degradation of ammonia nitrogen by Z-scheme NH2-MIL-101(Fe)/BiVO4 heterostructures, *J. Alloys Compd.*, 2023, **933**, 167815, DOI: 10.1016/j.jallcom.2022.167815.

57 S. K. Selahle, A. Mpupa and P. N. Nomngongo, Liquid chromatographic determination of per-and polyfluoroalkyl substances in environmental river water samples, *Arabian J. Chem.*, 2022, 103960.

58 N. Zhang, Y. Huang and M. Wang, 3D ferromagnetic graphene nanocomposites with ZnO nanorods and Fe3O4 nanoparticles co-decorated for efficient electromagnetic wave absorption, *Composites, Part B*, 2018, **136**, 135–142.

59 M. Wen, K. Mori, T. Kamegawa and H. Yamashita, Amine-functionalized MIL-101(Cr) with imbedded platinum nanoparticles as a durable photocatalyst for hydrogen production from water, *Chem. Commun.*, 2014, **50**(79), 11645–11648.

60 H. Shi, C. Li, L. Wang, W. Wang and X. Meng, Selective reduction of nitrate into N2 by novel Z-scheme NH2-MIL-101(Fe)/BiVO4 heterojunction with enhanced photocatalytic activity, *J. Hazard. Mater.*, 2022, **424**, 127711, DOI: 10.1016/j.jhazmat.2021.127711.

61 P. Azmoon, M. Farhadian, A. Pendashteh and S. Tangestaninejad, Adsorption and photocatalytic degradation of oilfield produced water by visible-light driven superhydrophobic composite of MIL-101(Cr)/Fe3O4-SiO2: Synthesis, characterization and optimization, *Appl. Surf. Sci.*, 2023, **613**, 155972, DOI: 10.1016/j.apsusc.2022.155972.

62 Y.-H. Chuang, S. Chen, C. J. Chinn and W. A. Mitch, Comparing the UV/monochloramine and UV/free chlorine advanced oxidation processes (AOPs) to the UV/hydrogen peroxide AOP under scenarios relevant to potable reuse, *Environ. Sci. Technol.*, 2017, **51**(23), 13859–13868.

63 S. Abdpour, *et al.*, Amino-functionalized MIL-101(Cr) photodegradation enhancement by sulfur-enriched copper sulfide nanoparticles: An experimental and DFT study, *J. Mol. Liq.*, 2020, **319**, 114341, DOI: 10.1016/j.molliq.2020.114341.

64 F. Chen, S. Xie, X. Huang and X. Qiu, Ionothermal synthesis of Fe3O4 magnetic nanoparticles as efficient heterogeneous Fenton-like catalysts for degradation of organic pollutants with H2O2, *J. Hazard. Mater.*, 2017, **322**, 152–162.

65 H. Li, *et al.*, Ammonia-nitrogen removal from water with gC3N4-rGO-TiO2 Z-scheme system *via* photocatalytic nitrification-denitrification process, *Environ. Res.*, 2022, **205**, 112434.

66 M. R. Billany, K. Khatib, M. Gordon and J. K. Sugden, Alcohols and ethanolamines as hydroxyl radical scavengers, *Int. J. Pharm.*, 1996, **137**(2), 143–147.

67 H. Ali, *et al.*, Solid-state synthesis of direct Z-scheme Cu2O/WO3 nanocomposites with enhanced visible-light photocatalytic performance, *Catalysts*, 2021, **11**(2), 293.

68 L. C. Makola, S. Moeno, C. N. M. Ouma and L. N. Dlamini, MXene mediated layered 2D-2D-3D g-C3N4@Ti3C2T@WO3 multijunctional heterostructure with enhanced photoelectrochemical and photocatalytic properties, *Nano-Struct. Nano-Objects*, 2023, **33**, 100934, DOI: 10.1016/j.nanoso.2022.100934.

69 T. Xiao, Z. Tang, Y. Yang, L. Tang, Y. Zhou and Z. Zou, In situ construction of hierarchical WO3/g-C3N4 composite hollow microspheres as a Z-scheme photocatalyst for the degradation of antibiotics, *Appl. Catal., B*, 2018, **220**, 417–428.

70 J. Hirayama and Y. Kamiya, Combining the photocatalyst Pt/TiO2 and the nonphotocatalyst SnPd/Al2O3 for effective photocatalytic purification of groundwater polluted with nitrate, *ACS Catal.*, 2014, **4**(7), 2207–2215.

71 J. Dong, Y. Shi, C. Huang, Q. Wu, T. Zeng and W. Yao, A new and stable Mo-Mo2C modified g-C3N4 photocatalyst for efficient visible light photocatalytic H2 production, *Appl. Catal., B*, 2019, **243**, 27–35.

72 X. Xue, *et al.*, Type-I SnSe2/ZnS heterostructure improving photoelectrochemical photodetection and water splitting, *Sci. China Mater.*, 2023, **66**(1), 127–138.

73 W. Li, J. Chen, R. Guo, J. Wu, X. Zhou and J. Luo, Facile fabrication of a direct Z-scheme MoO 3/Ag 2 CrO 4 composite photocatalyst with improved visible light photocatalytic performance, *J. Mater. Sci.: Mater. Electron.*, 2017, **28**, 15967–15979.

74 M. V. Krishna, G. Madhavi, N. F. Idris, S. A. M. Idris and L. R. K. Chowdary, Photocatalysis of b-blockers–An overview, *Arabian J. Chem.*, 2019, **12**, 1290–1297.

75 A. Ponkshe and P. Thakur, Solar light–driven photocatalytic degradation and mineralization of beta blockers propranolol and atenolol by carbon dot/TiO 2 composite, *Environ. Sci. Pollut. Res.*, 2022, **29**, 15614–15630.

76 J. G. Piedra López, O. H. González Pichardo, J. A. Pinedo Escobar, D. A. de Haro del Río, H. Inchaurregui Méndez

and L. M. González Rodríguez, Photocatalytic degradation of metoprolol in aqueous medium using a TiO2/natural zeolite composite, *Fuel*, 2021, **284**, 119030, DOI: 10.1016/j.fuel.2020.119030.

77 K. Kovács, T. Tóth and L. Wojnárovits, Evaluation of advanced oxidation processes for β-blockers degradation: a review, *Water Sci. Technol.*, 2022, **85**(2), 685–705.

78 V. K. Marothu, M. Gorrepati, N. F. Idris, S. A. M. Idris and R. K. C. Lella, Photocatalysis of β-blockers – An overview, *Arabian J. Chem.*, 2019, **12**(7), 1290–1297, DOI: 10.1016/j.arabjc.2014.10.044.

79 H. Yang, G. Li, T. An, Y. Gao and J. Fu, Photocatalytic degradation kinetics and mechanism of environmental pharmaceuticals in aqueous suspension of TiO2: A case of sulfa drugs, *Catal. Today*, 2010, **153**, 200–207.

80 N. Stojilovic, *et al.*, Synthesis and Characterization of Titania-Based Nanopowders for Photocatalytic Degradation of Pindolol, *Bull. Am. Phys. Soc.*, 2017, **62**, 18.

81 A. Ponkshe and P. Thakur, Significant mineralization of beta blockers Propranolol and Atenolol by TiO2 induced photocatalysis, *Mater. Today: Proc.*, 2019, **18**, 1162–1175.

82 J. Benner, E. Salhi, T. Ternes and U. von Gunten, Ozonation of reverse osmosis concentrate: Kinetics and efficiency of beta blocker oxidation, *Water Res.*, 2008, **42**(12), 3003–3012.

83 K. S. Tay and N. S. B. Ismail, Degradation of β-blockers in water by sulfate radical-based oxidation: kinetics, mechanism and ecotoxicity assessment, *Int. J. Environ. Sci. Technol.*, 2016, **13**, 2495–2504.

84 Y. Wang, X. Zeng and S. Shu, Theoretical study on the degradation mechanism of propranolol in aqueous solution initiated by hydroxyl and sulfate radicals, *Comput. Theor. Chem.*, 2022, **1217**, 113924.

85 K. Govindan, V. D. W. Sumanasekara and A. Jang, Mechanisms for degradation and transformation of β-blocker atenolol *via* electrocoagulation, electro-Fenton, and electro-Fenton-like processes, *Environ Sci (Camb)*, 2020, **6**(5), 1465–1481.

86 X. Liu, T. Zhang, Y. Zhou, L. Fang and Y. Shao, Degradation of atenolol by UV/peroxymonosulfate: kinetics, effect of operational parameters and mechanism, *Chemosphere*, 2013, **93**(11), 2717–2724.

87 A. Pinedo, M. López, E. Leyva, B. Zermeño, B. Serrano and E. Moctezuma, Photocatalytic decomposition of metoprolol and its intermediate organic reaction products: kinetics and degradation pathway, *Int. J. Chem. React. Eng.*, 2016, **14**(3), 809–820.

88 V. Píšťková, M. Tasbihi, M. Vávrová and U. L. Štangar, Photocatalytic degradation of β-blockers by using immobilized titania/silica on glass slides, *J. Photochem. Photobiol., A*, 2015, **305**, 19–28.

89 H. Yang, G. Li, T. An, Y. Gao and J. Fu, Photocatalytic degradation kinetics and mechanism of environmental pharmaceuticals in aqueous suspension of TiO2: A case of sulfa drugs, *Catal. Today*, 2010, **153**(3–4), 200–207.

90 Y. Chen, Z. Liu, Z. Wang, M. Xue, X. Zhu and T. Tao, Photodegradation of propranolol by Fe (III)–citrate complexes: kinetics, mechanism and effect of environmental media, *J. Hazard. Mater.*, 2011, **194**, 202–208.

91 C. M. B. Neves, *et al.*, Photodegradation of metoprolol using a porphyrin as photosensitizer under homogeneous and heterogeneous conditions, *J. Hazard. Mater.*, 2019, **370**, 13–23.

92 Z. Bensaadi, N. Yeddou-mezenner, M. Trari and F. Medjene, *J. Environ. Chem. Eng.*, 2014, **2**, 1371–1377, DOI: 10.1016/j.jece.2014.03.025.

93 A. K. Mohamed and M. E. Mahmoud, Metoprolol beta-blocker decontamination from water by the adsorptive action of metal-organic frameworks-nano titanium oxide coated tin dioxide nanoparticles, *J. Mol. Liq.*, 2020, **309**, 113096.

94 Y. Ji, C. Zeng, C. Ferronato, J.-M. Chovelon and X. Yang, Nitrate-induced photodegradation of atenolol in aqueous solution: kinetics, toxicity and degradation pathways, *Chemosphere*, 2012, **88**(5), 644–649.

95 A. Rey, D. H. Quinones, P. M. Álvarez, F. J. Beltrán and P. K. Plucinski, Simulated solar-light assisted photocatalytic ozonation of metoprolol over titania-coated magnetic activated carbon, *Appl. Catal., B*, 2012, **111**, 246–253.

96 V. Bhatia, G. Malekshoar, A. Dhir and A. K. Ray, Enhanced photocatalytic degradation of atenolol using graphene TiO2 composite, *J. Photochem. Photobiol., A*, 2017, **332**, 182–187.

97 A. Kowalczyk, B. Zgardzińska, K. Osipiuk, K. Jędruchniewicz, K. Tyszczuk-Rotko, M. Goździuk, H. Wang and B. Czech, The visible-light-driven activity of biochar-doped TiO2 photocatalysts in β-blockers removal from water, *Materials*, 2023, **16**(3), 1094.